

RESEARCH ARTICLE

10.1029/2018JB016132

Key Points:

- Dynamic weakening of wet gouges occurs at slip rates ≥ 40 mm/s at the onset of slip under conditions suppressing bulk fluid pressurization
- The onset of dynamic weakening is always contemporaneous with instantaneous dilatancy
- Flash weakening triggered by water vaporization around asperities and the resultant local pressurization may cause rapid dynamic weakening

Supporting Information:

- Supporting Information S1
- Data Set S1

Correspondence to:

L. Yao,
yaolu_cug@163.com;
luyao@ies.ac.cn

Citation:

Yao, L., Ma, S., Chen, J., Shimamoto, T., & He, H. (2018). Flash heating and local fluid pressurization lead to rapid weakening in water-saturated fault gouges. *Journal of Geophysical Research: Solid Earth*, 123, 9084–9100. <https://doi.org/10.1029/2018JB016132>

Received 25 MAY 2018

Accepted 11 SEP 2018

Accepted article online 14 SEP 2018

Published online 3 OCT 2018

Flash Heating and Local Fluid Pressurization Lead to Rapid Weakening in Water-Saturated Fault Gouges

Lu Yao¹ , Shengli Ma¹ , Jianye Chen² , Toshihiko Shimamoto¹ , and Honglin He³ 

¹State Key Laboratory of Earthquake Dynamics, Institute of Geology, China Earthquake Administration, Beijing, China, ²HPT Laboratory, Department of Earth Sciences, Utrecht University, Utrecht, The Netherlands, ³Key Laboratory of Active Tectonics and Volcano, Institute of Geology, China Earthquake Administration, Beijing, China

Abstract Coseismic fault displacement is quite large at shallow depths in some earthquakes, and it implies that fault gouges and sediments have extremely low dynamic friction during seismic slip. However, the dynamic weakening mechanisms of gouges under wet conditions are still not well constrained. Here we present direct evidence for the occurrence of flash heating and local fluid pressurization in water-saturated gouges, by performing low- to high-velocity ($V = 10 \mu\text{m/s}$ to 1 m/s) friction experiments in a pressure vessel, under conditions specially designed to suppress weakening effects of bulk thermal and compaction-induced pressurization. The tested gouges exhibit transition from velocity strengthening to drastic velocity weakening as slip rates increase. Strong dynamic weakening starts to occur at $V \geq 0.04$ m/s at the initiation of sliding ($< \sim 0.1$ m), which is much more efficient than previously reported in terms of the weakening velocity and distance. Furthermore, the onset of weakening is always accompanied by an instantaneous dilatancy (10–25 μm), which is much larger than that observed in dry tests and in contrast with gradual changes displayed in the wet tests without dynamic weakening. Numerical modeling integrated with microstructural observation reveals that bulk thermal pressurization cannot explain the experimental results, while flash weakening triggered by vaporization of water layers on/around asperity contacts and the resultant local fluid pressurization may be responsible for the observed rapid weakening concomitant with instantaneous dilatancy. Given high efficiency of such weakening process, fluid-infiltrated faults could be weakened more rapidly than previously recognized during seismic slip.

1. Introduction

Although shallow portions of mature fault zones are usually rich in clay minerals and frictionally stable at low slip rates, the propagation of earthquakes through these regions has been suggested to be energetically favorable (e.g., Faulkner et al., 2011; Togo et al., 2016; Ujiie et al., 2013). Two typical examples are the 2008 M_w 7.9 Wenchuan earthquake and the 2011 M_w 9.0 Tohoku-Oki earthquake, which both have large fault movements within gouges or sediments at shallow depth (maximum surface or seafloor displacements are ~ 10 m [Liu-Zeng et al., 2009] and ~ 50 m [Fujiwara et al., 2011], respectively). A closely related observation is that borehole temperature measurement directly after these earthquakes reveals very low temperature anomalies around slip zones (Fulton et al., 2013; Li et al., 2015), suggesting extremely low friction coefficient during the earthquakes (e.g., 0.08 for the Tohoku-Oki earthquake [Fulton et al., 2013]). Recent high-velocity friction experiments on water-saturated gouges have observed low peak and steady state friction, small slip weakening distance, and low fracture energy (Boulton et al., 2017; Chen, Niemeijer, Yao, et al., 2017; Faulkner et al., 2011; Ferri et al., 2010; Kitajima et al., 2011; Oohashi et al., 2015; Togo et al., 2016; Ujiie et al., 2013; Ujiie & Tsutsumi, 2010). These frictional properties favor seismic propagation and roughly accord with the low fault friction constrained from temperature records in fast drilling projects.

Thermal pressurization, compaction-induced pressurization, and flash heating were previously recognized to be dominant mechanisms in causing dynamic weakening in wet gouges (Faulkner et al., 2011; Kitajima et al., 2011; Oohashi et al., 2015). Of these mechanisms, flash heating on asperity contacts has been suggested to be very effective for most rocks at the early stages of slip (e.g., Beeler et al., 2008; Brantut & Platt, 2017; Goldsby & Tullis, 2011; Kohli et al., 2011; Passelègue et al., 2014; Proctor et al., 2014; Rice, 2006; Tisato et al., 2012; Violay et al., 2015; Yao et al., 2016). Under room humidity conditions, flash heating has been validated by well-designed experiments (Goldsby & Tullis, 2011) and plenty of mineralogical

evidence (e.g., mineralogical changes occurring at bulk temperatures much lower than what the reactions require [Oohashi et al., 2011; Viti & Hirose, 2010]). Under water-saturated conditions, for cohesive rocks, flash heating is thought to be much more efficient than thermal pressurization (TP; Violay et al., 2015). However, for incohesive rocks like fault gouges, the assessment of flash heating in the presence of water becomes difficult due to the superimposition of multiple mechanisms. Thermal and compaction-induced pressurization have been suggested as important weakening mechanisms for water-saturated gouges in modeling and experimental studies (e.g., Chen, Yang, Duan, et al., 2013; Faulkner et al., 2011; Kitajima et al., 2011; Noda & Shimamoto, 2005; Oohashi et al., 2015; Wibberley & Shimamoto, 2005), while there is rare evidence to support the occurrence of flash heating in this case besides theoretical expectation. Moreover, in previous studies, the detailed procedures for performing wet gouge experiments are quite variable in terms of the amount and distribution of water, the pretreatment of the gouge (with or without precompaction and preshear), the types of host rocks (permeable or impermeable), the confinement conditions (drained or undrained), and so on. These aspects make big differences in the observed frictional behavior (e.g., Chen, Niemeijer, Yao, et al., 2017; Faulkner et al., 2011) and thus hinder us from a better understanding of related weakening mechanism(s).

In this study, we devised low- to high-velocity friction experiments to explore the role of flash heating in dynamic weakening of water-saturated gouges, employing a newly designed pressure vessel. In each experiment, we imposed a water pressure of 2.0 MPa on a gouge layer sandwiched between two porous ceramic blocks (permeability of $1.4 \times 10^{-14} \text{ m}^2$) and applied a long preslip of 1.0 m in displacement before shearing at the target slip rates. The elevated water pressure raises the phase transition temperature of pore water to at least 212 °C, which can delay the weakening by water vaporization (if it occurs; Chen, Niemeijer, & Fokker, 2017). The use of highly permeable host blocks further facilitates fluid communication between the gouge layer and the vessel chamber, promoting the drainage of pore water when TP occurs. The long preslip imposed ensures good compaction and homogenized water distribution in the gouge layer. With all these designs and treatment, we could (1) slow down the bulk TP process and (2) suppress or even eliminate the pressurization due to sudden compaction especially at the very beginning of experiments. Therefore, the role of flash heating may get a chance to stand out.

2. Samples and Methods

2.1. Geological Background, Fault Zone Structure, and Gouge Materials

Experiments were performed on a granular gouge and a clay-rich gouge both collected from a surface outcrop of the Qingchuan fault (Sun et al., 2015), which is the northeastern segment of the Longmenshan fault system at the eastern margin of the Tibetan Plateau. Figure 1a shows the map view of the Qingchuan fault (rose-red lines), including the surface rupture associated with the 2008 Wenchuan earthquake (dark-gray lines). The Qingchuan fault exposes at the Guangping town (hereafter referred to as Guangping outcrop; Figure 1b) with a width of ~140 m, consisting of several units of fault breccias and gouges (see details of the entire fault zone in the supporting information). The fault core is 5 m wide perpendicular to the fault plane (Figure 1c; the apparent width is much larger since the orientation of the exposure is close to the fault strike of N60°E). From east to west, the fault core consists of a brown-colored granular gouge layer (Unit 2 in Figures 1c and 1d; weakly solidified and about 0.2 m wide; referred to as granular gouge hereafter), a gray-blue-colored clay-rich gouge layer (Unit 3 in Figures 1c and 1d; 3.2 m wide; referred to as clay-rich gouge hereafter) and a gray foliated fault breccia zone (Unit 4 in Figure 1c; 1.6 m wide). Important discovery from the field observation is that a fault plane (dipping angle, 70° NW) with striations is located within the granular gouge (see the flat fault surface in Figures 1d and 1e).

The two representative fault gouges (the sampling locations were indicated by yellow ellipses in Figure 1d) were chosen as the starting materials for our friction experiments. X-ray diffraction analysis indicate that the granular gouge contains 20% quartz, 18% plagioclase, 17% calcite, 15% illite, 12% smectite, 5% microcline, 5% hornblende, 4% chlorite, and 4% pyrite, while the clay-rich gouge contains 47% illite, 17% quartz, 14% chlorite, 13% plagioclase, 5% microcline, and 4% smectite. The fault gouges were carefully sieved to achieve a grain-size fraction of $<150 \mu\text{m}$. Laser grain size analysis indicated that the median grain sizes (d_{50}) of the granular and clay-rich gouges were 14.5 and 4.5 μm , respectively (see cumulative grain size distributions in Figure S2 in the supporting information).

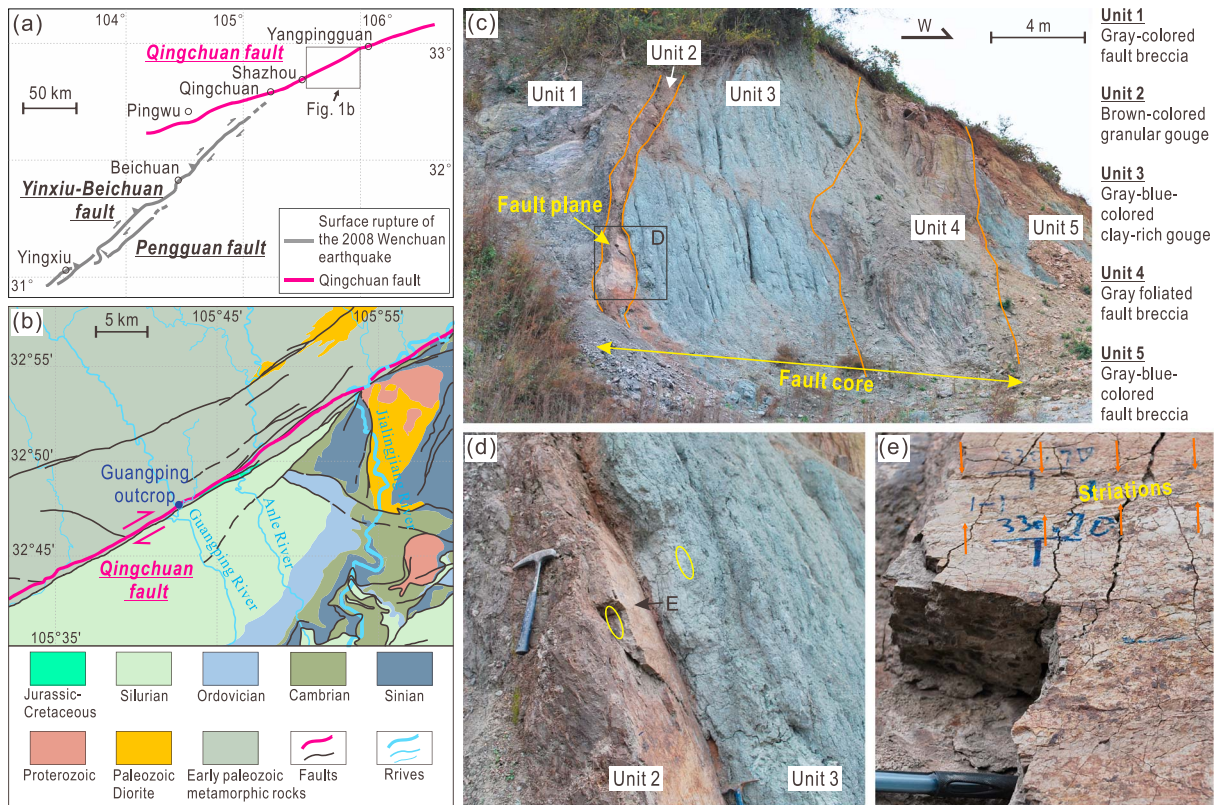


Figure 1. Geological setting and internal structures of the Qingchuan fault (the northeastern segment of the Longmenshan fault system at the eastern margin of the Tibetan Plateau) at Guangping outcrop, where the tested granular and clay-rich fault gouges were collected. (a) Simplified map showing location of the Qingchuan fault. (b) Geological map of the region near the Guangping outcrop. (c) Photograph showing fault zone structures and fault rocks near the fault core. (d, e) Photographs of the fault plane. Sampling locations of the two gouges are indicated by yellow ellipses in Figure 1d.

2.2. Experimental Procedure

We performed friction experiments in a low- to high-velocity rotary shear apparatus equipped with a pressure vessel (Ma et al., 2014; Figure 2a). The vessel is mainly designed for rock-on-rock type experiments, and its main parts are shown in Figure 2b (see detailed description in Ma et al., 2014). With the use of highly permeable ceramic host blocks, we could perform gouge experiments under pore pressure using the common assembly (Figure 2c). In each experiment, 2.2-g gouge was flooded with deionized water and then sandwiched (~1 mm thick) between two ceramic cylinders (39.980 mm in diameter), with a Teflon sleeve fitting tightly around the gouge layer. The whole sample assembly was placed in sample holders in the pressure vessel, and deionized water was added to fill the vessel after it was mounted on the apparatus. A constant background fluid pressure (P_f) of 2.0 MPa was then applied by pressurized high purity nitrogen through a pore pressure generating system (up to 40 MPa). The normal load was applied by an air actuator to generate an effective normal stress ($\sigma_{n,eff}$) of 1.3–1.5 MPa. All the experiments were started from a 1.0-m-long preslip at a slip rate $V = 5$ mm/s except one comparative experiment. After the preslip, the experiments were paused to reset the motor speeds to target values ($V = 10$ μ m/s to 1.0 m/s) and then were continued toward total shear displacements of 3.0–3.6 m for $V \leq 100$ mm/s or of 11–12 m for $V = 0.4$ –1.0 m/s.

The Teflon sleeve functioned well in our experiments (much better than the dry experiments), and in most cases the gouges barely leaked. As the short-term fluctuations of measured torque mainly result from misalignment of specimens and Teflon sleeve, it is helpful to smooth data by taking moving average of the data recorded in one revolution of specimen (e.g., Yao et al., 2013). From one test conducted under a series of normal stresses (0.4–1.7 MPa), the apparent shear stress due to Teflon friction was estimated as 0.037 MPa (the intercept in the plot of shear and normal stresses; Togo et al., 2011). All the mechanical data have been corrected accordingly.

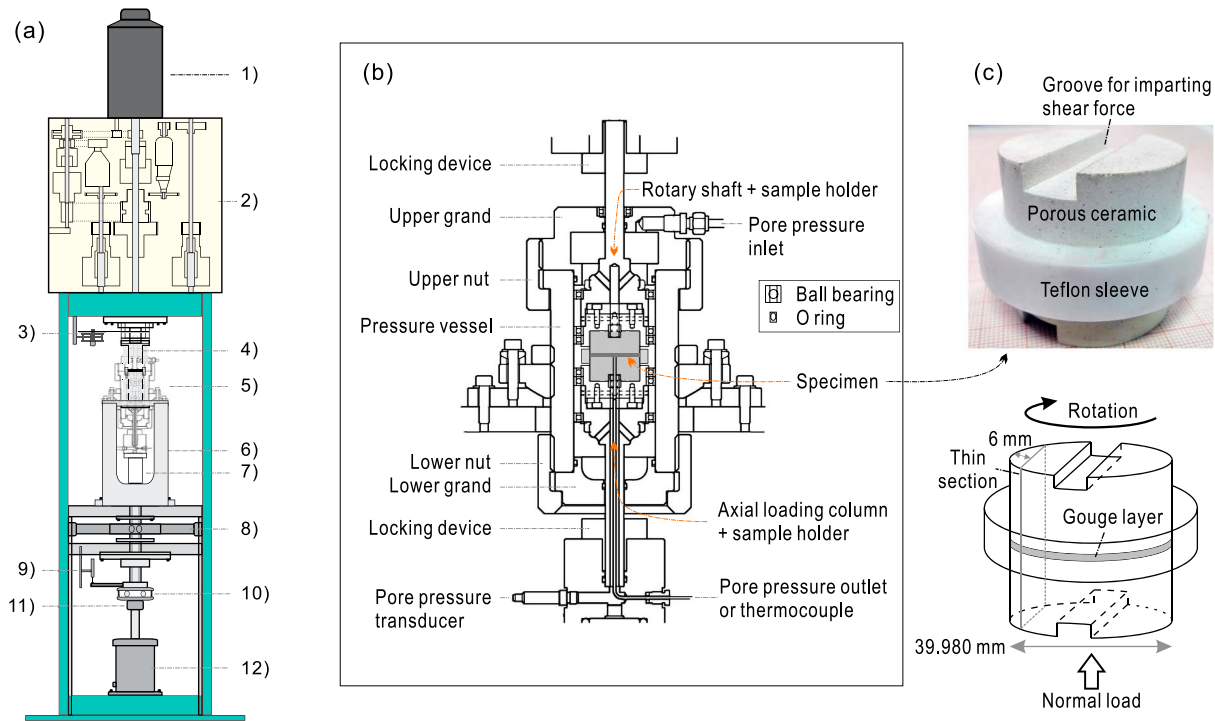


Figure 2. Experimental apparatus and sample assembly. (a) A schematic diagram of the low- to high-velocity rotary shear apparatus at Institute of Geology, China Earthquake Administration (Ma et al., 2014). 1) servomotor, 2) gear and belt system for changing velocity, 3) rotary encoder and potentiometer, 4) rotary shaft, 5) pressure vessel, 6) metal frame for fixing the pressure vessel, 7) axial loading column, 8) cantilever-type torque gauge, 9) axial displacement transducer, 10) thrust bearing, 11) axial force gauge, and 12) air actuator. (b) A diagram exhibiting main parts of the pressure vessel (after Ma et al., 2014). (c) The sample assembly with gouge layer, Teflon sleeve and host blocks made of highly permeable porous ceramic.

3. Experimental Results

Figure 3 shows the evolution of friction coefficient with displacement for nine experiments on the granular gouge (Figure 3a) and eight experiments on the clay-rich gouge (Figure 3b). Each experiment consists of a 1-m-long preslip and a main slip sequence. The frictional behavior during the first 0.3 m of preslip was highly varied from test to test due to differences in the initial compaction, but the friction coefficients (μ) show high reproducibility in later stages of the preslip. To the comparison purpose, here we only show the data at shear displacements of 0.4–3.2 m.

The two gouges both exhibit a diverse range of frictional behaviors in main slip sequences under different slip velocities. For the granular gouge, the steady state friction coefficient (μ_{ss}) slightly increases from 0.39 at $V = 100 \mu\text{m/s}$ to 0.43 at $V = 10 \text{ mm/s}$. However, at $V \geq 40 \text{ mm/s}$, μ decreases suddenly at the onset of slip. For instance, μ reduces by 0.17, 0.18, 0.20, and 0.28 within 0.02 m of slip at $V = 40 \text{ mm/s}$, 100 mm/s , 0.4 m/s , and 1.0 m/s , respectively, with further gradual weakening as slip proceeds (Figure 3a). The fluctuations of friction at $V = 0.4$ and 1.0 m/s become smaller at longer displacement (Figure 4a), and μ_{ss} at these two velocities is as low as 0.06.

For the clay-rich gouge, μ_{ss} increases from 0.24 to 0.34 as V increases from $10 \mu\text{m/s}$ to 100 mm/s (Figure 3b), indicating a clear trend of velocity strengthening. For the experiments at $V = 0.4$ and 1.0 m/s , the data presented in Figure 3b are only the initial portions for the purpose of comparison. The entire evolution of friction in these two experiments (shown in Figure 4b) is characterized by a sharp weakening (μ decreases by about 0.16–0.24 mostly within 0.25 m of slip), followed by a quick strengthening (μ increases by 0.25–0.28) and a modest weakening (μ decreases by 0.07–0.16) as sliding proceeds.

Dramatic weakening at the onset of slip occurs in the case of $V \geq 40 \text{ mm/s}$ for the granular gouge and $V \geq 0.4 \text{ m/s}$ for the clay-rich gouge (Figure 3). To understand what happened within the gouge layers during the weakening, we plotted the data of frictional coefficient together with axial displacement in Figures 4a–4d.

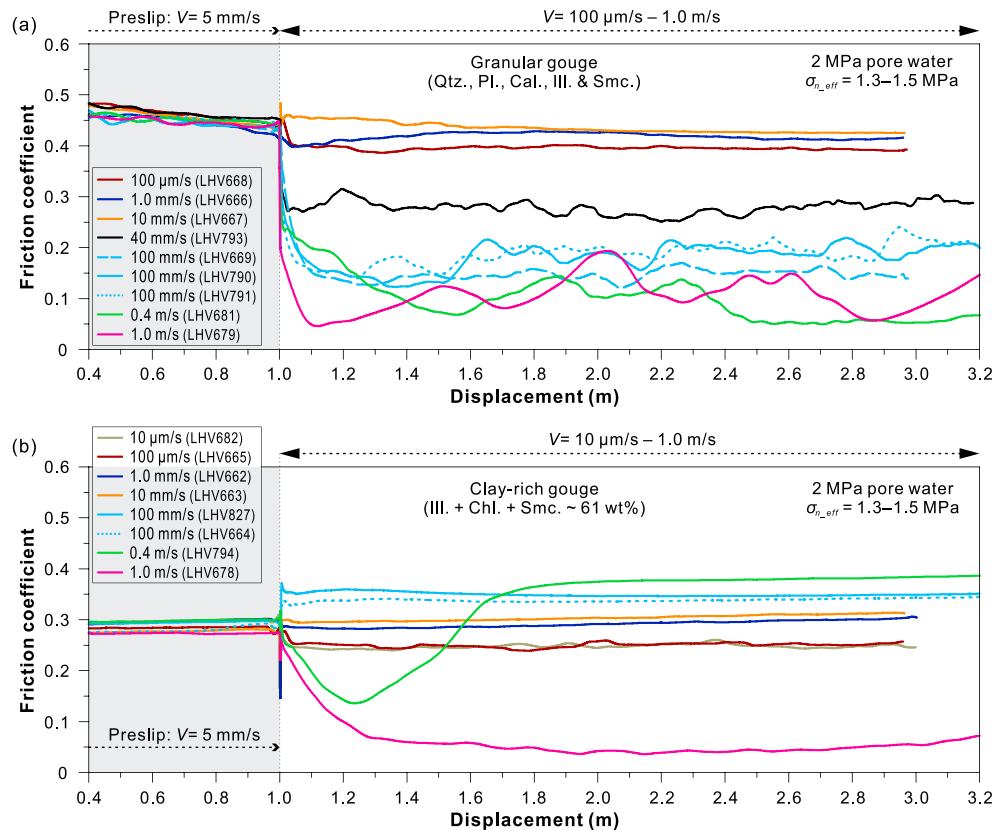


Figure 3. Low- to high-velocity frictional behaviors of the granular gouge (a) and the clay-rich gouge (b). The experiments were performed at an effective normal stress σ_{n_eff} of 1.3–1.5 MPa under pore water pressure of 2 MPa. Each experiment here started from a preslip of 1.0 m at a slip rate $V = 5$ mm/s and then resumed at various V ranging from 10 μ m/s to 1.0 m/s.

One interesting observation is that the initial sharp weakening is always contemporaneous with an axial dilatancy of 10–25 μ m for both of the gouges (yellow-colored region in Figures 4a–4c). Two repeated experiments confirm the reproducibility of this coincidence (solid and dashed blue lines in Figure 4c). In contrast, for those tests that do not exhibit sharp initial weakening (i.e., $V \leq 10$ mm/s for the granular gouge and $V \leq 100$ mm/s for the clay-rich gouge), there is no visible instantaneous change in the axial displacement at the onset of slip (orange lines in Figure 4c and lines in Figure 4d). Another interesting observation is that the friction evolution following the initial weakening is accompanied by axial shortening for the granular gouge, while by continued dilatancy for the clay-rich gouge (cf. Figures 4a–4c).

We further performed two control experiments with respect to the standard tests shown in Figure 3. One was performed without the preslip, and the other was under room humidity (both at $V = 100$ mm/s and $\sigma_{n_eff} = \sim 1.3$ MPa). The former reveals a large amount of compaction prior to peak friction (~ 0.35 -mm axial shortening) and a 1.5-m-long slip weakening distance that is ~ 10 times of that observed in the standard tests (Figure 4c). The latter shows a small dilatancy at the initiation of slip (~ 4 μ m) along with high friction ($\mu = 0.60$ to 0.65), which is in contrast to the relatively large initial dilatancy (~ 20 μ m) and the rapid weakening observed in the standard tests (cf. purple and blue lines in Figure 4e). These two control tests strongly suggest the potential links between the observed initial weakening, the instantaneous dilatancy and the presence of water in the wet experiments.

4. Microstructures

Figure 5 compares representative microstructures of the granular gouge between the starting gouge layer (Figure 5a), the presheared (Figure 5b), and the deformed gouge layers at various slip rates (Figures 5c–5h). The starting material after static compaction contains a large amount of quartz and plagioclase grains with

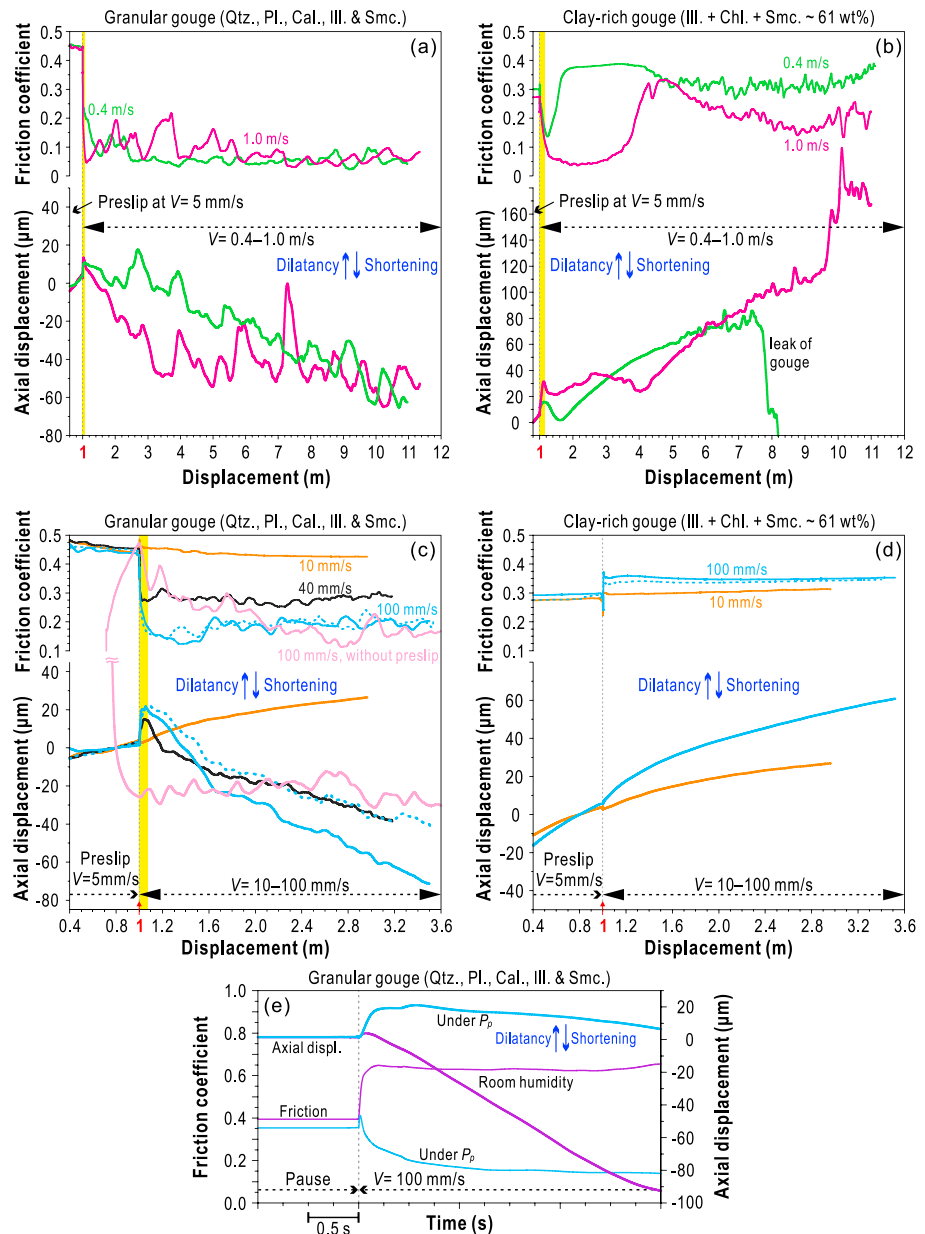


Figure 4. (a–d) Axial displacement and friction coefficient versus displacement results for the granular gouge (a, c) and the clay-rich gouge (b, d). (e) Comparison of the friction and axial displacement data of the granular gouge under room-humidity condition with that under water pressure (P_p) condition ($V = 100$ mm/s). The gray dashed line in each plot indicates the displacement at which the preslip at $V = 5$ mm/s was ended and the slip rate was reset to the target value. The yellow-colored regions in Figures 4a–4c highlight the instantaneous dilatancy that coincides with the sharp weakening at the onset of slip under prescribed velocities. Line colors in this figure correspond with Figure 3. For easy comparison, the axial displacement at shear displacement of 0.8 m was reset to 0 in the plots.

angular to subround shapes (Figure 5a). During the preslip, the grains adjacent to the rotary host block were crushed and a localized shear zone of 200 μm thick was formed (Figure 5b). As experiments proceed, the granular gouges deformed at various slip rates show two distinct kinds of microstructures. At $V \leq 10$ mm/s and $V \geq 0.4$ m/s, the whole gouge layers were involved in shear deformation without extremely localized slip zones, and few large grains were preserved after experiments (Figures 5c, 5d, 5g, and 5h). However, at $V = 40$ and 100 mm/s, remarkable grain size reduction is only observed within shear zones of 200–400 μm in thickness, leaving 50–70% of the gouge layers nearly undeformed (Figures 5e and 5f).

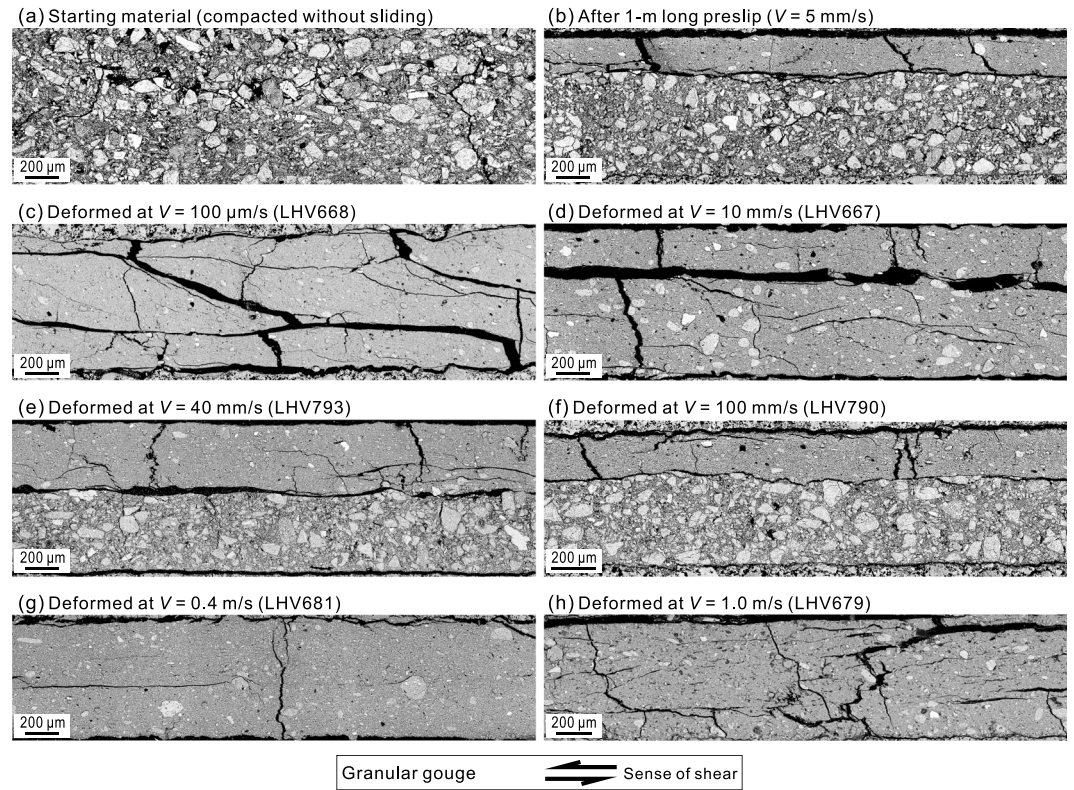


Figure 5. Backscattered electron images of the granular gouge. (a) The statically compacted gouge; (b) the presheared gouge at the slip rate (V) of 5 mm/s; (c–h) the experimentally deformed gouges at various slip rates of 100 $\mu\text{m/s}$, 10 mm/s, 40 mm/s, 100 mm/s, 0.4 m/s, and 1.0 m/s.

In contrast, the clay-rich gouge shows obviously different microstructures. The initial material contains much fewer coarse grains (subround to round shapes), exhibiting a matrix-supported structure (Figure 6a). Unlike the cases of the granular gouge, the deformed clay-rich gouges seem to undergo distributed shear over the entire gouge layers at all tested velocities (Figures 6b–6f). Compared with the simply compacted sample (Figure 6a), the microstructures of the deformed gouges are characterized by slight grain size reduction, preferred orientation of coarse grains and abundant P and Y fractures, and all these deformation textures seem not to vary with slip rates (Figures 6c–6f).

5. TP in Bulk Gouge Layer

The experiments were performed under fluid pressure, so TP of the bulk gouge layer is a potential dynamic weakening mechanism. We assessed this effect through numerical modeling following previous studies (Brantut et al., 2010; Chen, Yang, Duan, et al., 2013; Kitajima et al., 2011; Rice, 2006; Tanikawa et al., 2009). As temperature rises were not high in our experiments (Figures S3 and S4 in the supporting information), we ignore the contribution from dehydration reactions of the clay minerals. We also ignore the porosity changes in the modeling. Considering the fact that the initial weakening (we mainly concern about) is always accompanied by the gouge dilatancy, our results should give the upper-bound estimate on the weakening by TP. According to the energy and fluid mass conservation, the governing equations are

$$\rho c \frac{\partial T}{\partial t} = \nabla \cdot (\lambda \nabla T) + Q, \quad (1)$$

$$S_s \frac{\partial P}{\partial t} = \nabla \cdot \left(\frac{k}{\eta} \nabla P \right) + \varphi (\alpha_f - \alpha_m) \frac{\partial T}{\partial t}. \quad (2)$$

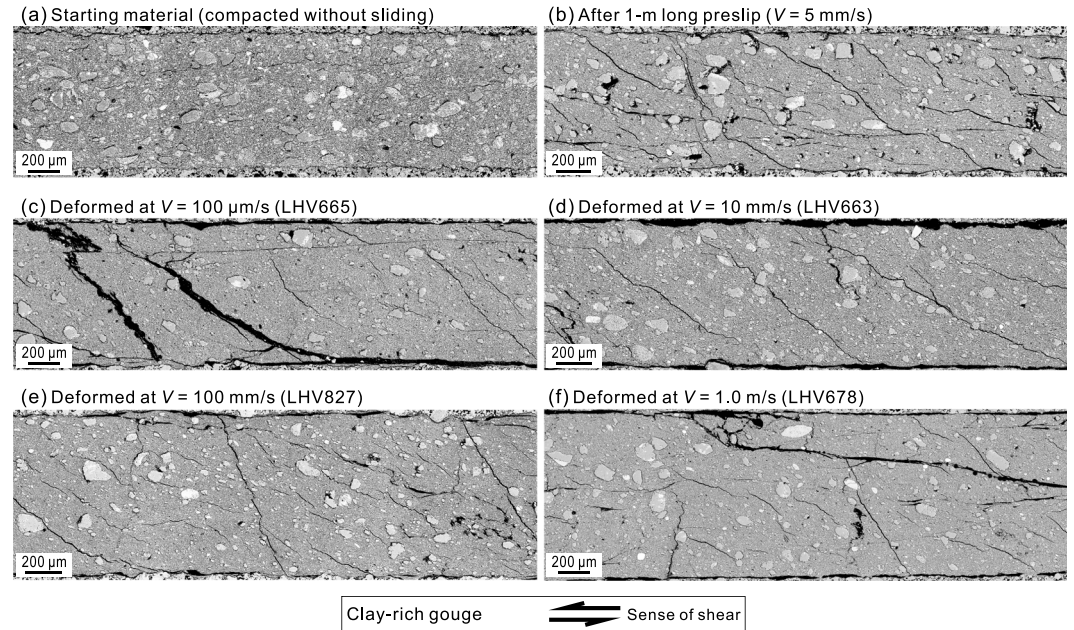


Figure 6. Backscattered electron images of the clay-rich gouge after static compaction (a), after the preslip at the slip rate (V) of 5 mm/s (b), and after the experiments at $V = 100 \mu\text{m/s}$, 10 mm/s, 100 mm/s, and 1.0 m/s (c–f).

Here T is the temperature, t is the time, λ is the thermal conductivity, ρ is the density, c is the specific heat capacity, and Q is the heat generation rate per unit volume. Further, P is the pressure, S_s is the specific storage, k is the permeability, η is the dynamic viscosity of fluid, α_f and α_m are thermal expansivities of the fluid and mineral matrix, and ϕ is the porosity.

In order to specify the heat source (Q), a proper assumption of intrinsic friction coefficient (μ_{in}) of gouge is indispensable. Previous studies assumed the μ_{in} of wet gouge as a constant value (e.g., Noda & Shimamoto, 2005), or a temperature-dependent value (e.g., Kitajima et al., 2011), or the friction coefficient measured in the dry tests (e.g., Chen, Yang, Duan, et al., 2013; Tanikawa et al., 2009). Here the μ_{in} is predicted by an updated flash heating model that incorporates the effects of bulk temperature rise and distributed shear within gouge layer (e.g., Brantut & Platt, 2017; Platt et al., 2014; Rempel, 2006), on the basis of Rice's original model (Rice, 2006). The characteristic weakening velocity (V_w) in this case is (Brantut & Platt, 2017; Platt et al., 2014)

$$V_w(T_f) = N_a * V_w^a(T_f) = N_a * \frac{\pi \alpha}{D_a} \left[\frac{\rho c (T_w - T_f)}{\tau_c} \right]^2, \quad (3)$$

where T_f is the bulk temperature of fault zone, N_a is the number of asperity contacts sharing the total slip velocity (V), V_w^a is the weakening velocity for the bare surface case, α is the thermal diffusivity, ρ is the density, c is the heat capacity, D_a is the diameter of asperity, T_w is the characteristic weakening temperature, and τ_c is the contact shear strength. At $V \leq V_w$, the friction coefficient $f = f_0$ (f in the unweakened state or at low slip rates). Flash weakening occurs at $V > V_w$ and f in this case is (Rice, 2006)

$$f = (f_0 - f_w) \frac{V_w}{V} + f_w, \quad (4)$$

where f_w is the f in the weakened state. We employed $\mu_{in} = f$ in the modeling. Based on the measured friction at the end of preslip and the minimum friction in the experiments, we set $f_0 = 0.44$ and $f_w = 0.057$ for the granular gouge, and $f_0 = 0.29$ and $f_w = 0.044$ for the clay-rich gouge. In the equation (3), values for T_w , τ_c , D_a , and N_a are not well known. While acknowledging the uncertainty involved, reasonable ranges of these parameters have been suggested in many studies (e.g., Goldsby & Tullis, 2011; Proctor et al., 2014; Rice, 2006). We

further constrained these parameters based on the mineralogical and microstructural characteristics of the two gouges (discussed below in section 6.3). This yields T_w , τ_c , D_a , and N_a of 1000 °C, 8 GPa, 5 μm , and 10 (4 in the case of localized shear), respectively, for the granular gouge, and of 300 °C, 2 GPa, 10 μm , and 10, respectively, for the clay-rich gouge.

Permeability (k) of the gouge layer is another decisive parameter. Here we quote the permeability data of experimentally deformed gouges reported in Oohashi et al. (2015), where both gouge samples and experimental conditions are comparable to ours. Then k of the sheared granular and clay-rich gouges are assumed to be $6 \times 10^{-20} \text{ m}^2$ (k of sheared smectite-quartz mixtures with smectite contents of $\sim 27\%$ in Oohashi et al., 2015) and $1 \times 10^{-20} \text{ m}^2$ (in consideration of its higher clay contents), respectively. To know the limitation of modeling due to rough estimate on k , we did some modeling using higher and lower k values ($\sim 10^{-18}$ and 10^{-21} m^2). The initial and boundary conditions in the modeling were set based on the real conditions in the experiments. The parameter setting of thermal (Brigaud & Vasseur, 1989; Clauser & Huenges, 1995; Schön, 2011; Skauge et al., 1983; Waples & Waples, 2004), hydraulic (Brace et al., 1968; Chen, Yang, Duan, et al., 2013; Chen, Yang, Yao, et al., 2013; Oohashi et al., 2015), and other related properties (<https://webbook.nist.gov/chemistry/fluid/>; <http://www.phy.davidson.edu/fachome/dmb/PY430/Friction/teflon.html>) are specified in the supporting information.

A 2-D axisymmetric geometrical model was built according to the sample assembly. We solved this coupled thermal-hydrological-mechanical problem using the finite-element package COMSOL. As is shown in Figures 7a and 7b, the TP modeling predicts slight decreases in equivalent friction at $V \leq 0.1 \text{ m/s}$ (black and blue lines) and gradual slip weakening at $V \geq 0.4 \text{ m/s}$ (green and red solid lines). Flash weakening occurs at $V = 1.0 \text{ m/s}$ for the granular gouge and at $V = 0.4$ and 1.0 m/s for the clay-rich gouge (see dashed lines), causing much lower friction than the low-velocity cases at the very beginning (green and red solid lines). The subsequent decreases in friction mostly result from the bulk TP. With higher and lower k values ($\sim 10^{-18}$ and 10^{-21} m^2), the modeling results provide possible ranges of behaviors caused by flash weakening and the TP in bulk gouge layers (Figures 7c and 7d; $V = 0.4$ and 1.0 m/s). In all the cases simulated, big differences exist between the modeled apparent μ and the measured μ at given displacements of 1.1, 1.2, 1.4, 3.0, 6.0, and 10.0 m (filled circles). For the granular gouge, the discrepancies exist in both early stages and final steady states for all the slip velocities. For the clay-rich gouge, the modeling results cannot explain the initial sharp weakening ($V \geq 0.4 \text{ m/s}$) that we mainly concern about, let alone the curious strengthening and weakening in the later stages, as we will discuss latter.

6. Discussion

6.1. Velocity Dependence of Friction and Rapid Weakening at Subseismic to Seismic Slip Rates: Implications to Seismic Faulting

Both of the tested gouges show velocity strengthening at $V \leq 10\text{--}100 \text{ mm/s}$ (Figure 8). The lower frictional strength of the clay-rich gouge at $V \leq 10 \text{ mm/s}$ could be explained by its higher contents of phyllosilicates ($\sim 65\%$ vs. 31% for the granular gouge; e.g., Zhang & He, 2013). Previous studies have reported similar velocity strengthening behaviors at slip rates less than or close to $10\text{--}100 \text{ mm/s}$ for various material and experimental conditions (Buijze et al., 2017; Ferri et al., 2011; Reches & Lockner, 2010; Sawai et al., 2014). This strengthening may act as a barrier to accelerating slip during seismic rupture propagation.

As the clay-rich gouge shows two stages of slip weakening separated by a strengthening stage at $V = 0.4$ and 1.0 m/s (Figure 4b), both of the μ_{ss} during the second slip weakening and the minimum friction coefficient during the initial weakening (μ_{min}) are plotted in Figure 8 for these two velocities. Dynamic weakening of the granular gouge occurs at $V \geq 40 \text{ mm/s}$, about 1 order of magnitude higher than that of the clay-rich gouge ($V \geq 0.4 \text{ m/s}$; Figure 8). In addition, at $V \geq 40 \text{ mm/s}$, the granular gouge has lower μ_{ss} than the clay-rich gouge. The lower V_w and μ_{ss} of the granular gouge imply a stronger role in promoting rupture propagation once seismic slip overcomes the barrier of the intermediate velocity strengthening. This is in line with the field observation at the studied Guangping outcrop that the slip surface is located within the narrow granular gouge zone (Unit 2 in Figure 1c) rather than the wide clay-rich gouge zone (Unit 3). This consistency suggests that frictional properties of fault rocks may exert an important control on seismic rupture propagation,

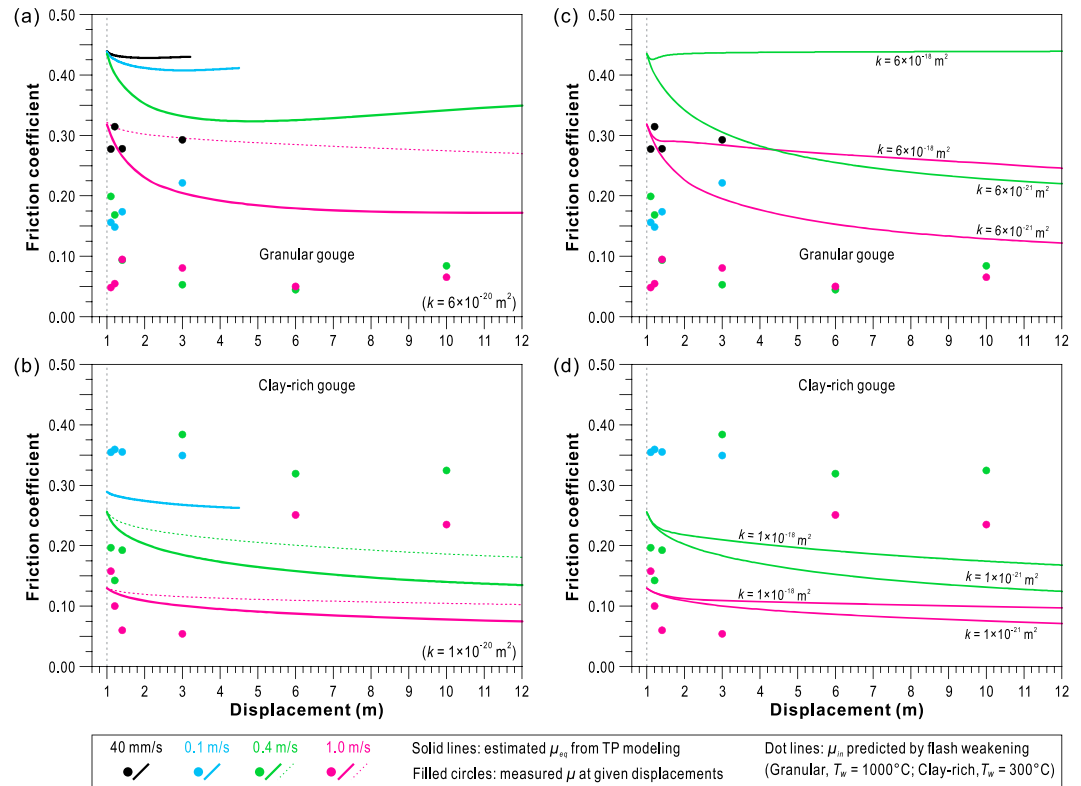


Figure 7. Comparison of the estimated equivalent friction coefficient (μ_{eq}) from thermal pressurization (TP) modeling (solid lines) with the measured frictional data (filled circles) at given displacements of 1.1, 1.2, 1.4, 3.0, 6.0, and 10.0 m. The permeability (k) of the two gouges under shear are assumed based on the published data (Oohashi et al., 2015) in consideration of a possible range. (a, b): $k \sim 10^{-20} \text{ m}^2$; (c, d): $k \sim 10^{-18}$ and $\sim 10^{-21} \text{ m}^2$. The dashed lines in Figures 7a and 7b show the evolution of intrinsic friction coefficients (μ_{in}) used in the TP modeling in the cases that meet flash weakening conditions. Colors of lines and circles denote slip rates.

providing a possible explanation for the selection of seismic slip zones and the development of wide gouge zones for mature faults.

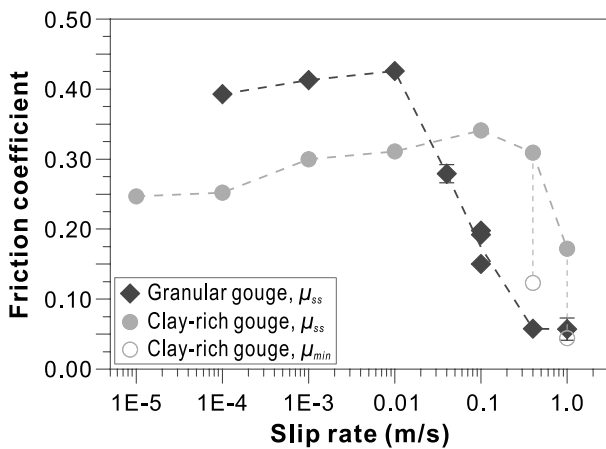


Figure 8. The steady state friction coefficient (μ_{ss}) as a function of slip velocity (V). The minimum friction coefficients of the clay-rich gouge during the initial sharp weakening (μ_{min}) at $V = 0.4$ and 1.0 m/s are also plotted for comparison.

It is noteworthy that the tested two gouges show extremely rapid weakening at the initiation of slip (within ~ 0.1 m) at $V \geq 0.04$ to 0.4 m/s. Previous workers have described that the wet gouges may weaken immediately with a negligible slip weakening distance (D_c) at high velocities (e.g., Faulkner et al., 2011). However, recent work showed that the slip weakening process of wet gouges might become much slower if the compaction-induced pressurization were suppressed by presliding (Boulton et al., 2017; Chen, Niemeijer, Yao, et al., 2017; Oohashi et al., 2015). The observed D_c in these studies is about one or a few meters at experimental conditions comparable to ours (e.g., Figure 3a in Oohashi et al., 2015, and Figure 1e in Chen, Niemeijer, Yao, et al., 2017). In our experiments, the pressurization effects due to initial compaction and frictional heating in the bulk gouge layer become ineffective at the initiation of slip. However, we even observe much shorter D_c at $V \geq 0.04$ to 0.4 m/s (0.1–0.25 m vs. one or a few meters previously reported), suggesting the operation of more efficient weakening mechanisms in our case (as discuss later). As mature faults usually contain existing highly deformed slip zones analogous to what we observed after the preslip (Figures 5b and 6b), we believe the similar rapid weakening process might occur in natural fault zones, which may play an important role in promoting seismic rupture propagation.

6.2. Analysis of the Instantaneous Dilatancy Accompanying the Sharp Weakening at the Initiation of Slip

Because the initial sharp weakening is always contemporaneous with the axial dilatancy of 10–25 μm , the causes of this dilatancy may provide hints on the weakening mechanisms. The potential factors that could explain the initial dilatancy include the thermal expansion of gouge layer, the unpacking of overconsolidated gouge layer (Lambe & Whitman, 1969; Marone et al., 1990) and the disturbance in effective normal stress (e.g., a sudden decrease in σ_{n_eff} due to an increase in pore pressure). The linear thermal expansivities of common minerals are 10^{-6} – 10^{-5} K^{-1} (Robertson, 1988; e.g., 1.66×10^{-5} and $7.5 \times 10^{-6} \text{ K}^{-1}$ for quartz and albite, respectively). During the first 0.1–0.4 m of slip, the temperature of bulk gouge layer remains low ($<100 \text{ }^\circ\text{C}$; supporting information). Given these thermal parameters and the gouge thickness of $\sim 1.0 \text{ mm}$, the axial dilatancy due to thermal expansion is expected to be less than $\sim 1 \text{ } \mu\text{m}$ during the short period of initial weakening.

A sheared gouge layer can dilate naturally if the shearing rate increases (Marone et al., 1990). To estimate this effect, we follow the constitutive equation for porosity of fault gouge proposed by Segall and Rice (1995). Taking the porosity during the preslip as the reference state and assuming a dilatancy coefficient of 1.7×10^{-4} (Segall & Rice, 1995), the estimated increases in porosity are 3.54×10^{-5} , 5.09×10^{-4} , 7.45×10^{-4} , and 9.01×10^{-4} for velocity jumps from 5 mm/s to 40 mm/s, 100 mm/s, 0.4 m/s, and 1.0 m/s, respectively. These changes in porosity correspond to increases in gouge thickness of $\sim 1 \text{ } \mu\text{m}$, which are much smaller than the observed axial dilatancy. Furthermore, there is no significant dilatancy in the control test under room humidity and in the wet tests that do not exhibit slip weakening (Figures 4c–4e). These analyses suggest that the instantaneous dilatancy cannot be explained by the initiation of shear on the presheared gouge layer. We propose the hypothesis that the initial dilatancy is due to an increase in local pore pressure caused by flash heating, which breaks the balance of effective normal load applied on the gouge layer, as discussed in the following section. According to the axial displacement data recorded in one experiment with the σ_{n_eff} varied from 0.44 to 1.71 MPa, a reduction in σ_{n_eff} of 0.2–0.5 MPa is probably sufficient to cause axial dilatancy of 10–25 μm in our experiments.

6.3. Flash Weakening Caused by Vaporization of Water Films (Layers) on/Round Asperities Contacts

The most intriguing observation in this work is that the drastic weakening occurs simultaneously with the obvious dilatancy immediately after the sliding commences ($V \geq 0.04$ – 0.4 m/s ; Figures 3 and 4). The small D_c of 0.1–0.25 m and the low V_w down to 0.04 m/s suggest that the dominant weakening mechanism(s) is/are very efficient. As the experimental conditions devised are unfavorable for fluid pressurization in the bulk gouge layer, we can exclude bulk TP as an effective mechanism accounting for the initial weakening, just as our modeling results demonstrate above. In addition, compaction-induced pressurization can also be excluded by the observation that the axial dilatancy rather than shortening accompanies the initial weakening. Although flash heating also seems to be insufficient to explain the observed weakening (dashed lines in Figure 7), what we considered in section 5 are actually the flash weakening by local melting of quartz/plagioclase ($T_w = 1000 \text{ }^\circ\text{C}$) and by local softening due to decomposition of illite ($T_w = 300 \text{ }^\circ\text{C}$), for the granular and clay-rich gouges, respectively. This is based on the concept of flash weakening that both local melting and thermal softening may cause weakening of asperity contacts (e.g., Kohli et al., 2011; Rice, 2006; Spagnuolo et al., 2015; Tisato et al., 2012; Tullis, 2015). If we further extend this concept, in the presence of pore water, we could expect that the vaporization of water layers (films) on/around contacts may resemble common thermal softening processes, which may lubricate the contacts and cause macroscopical weakening. One may think that the evaporation of water layers around contacts probably leads to higher friction (e.g., Sammis et al., 2011). Apart from the opposite view that the drainage of absorbed water layers may cause weakening (e.g., Mizoguchi et al., 2006), the water vaporization around asperities in our case seems to be very different from the desorption process of absorbed water layers surrounding dry solid grains. The point is that, in our experiments, the contacts may not become dry after the surrounding water layers are vaporized because of the large volume of pore water nearby. Instead, vaporization may significantly change physical properties of water layers on/around asperities, some of which such as viscosity is critical to friction on the contacts (e.g., Sammis et al., 2011). We propose that flash weakening triggered by water vaporization around asperities and the resultant local pressurization may explain the rapid dynamic weakening observed in our experiments.

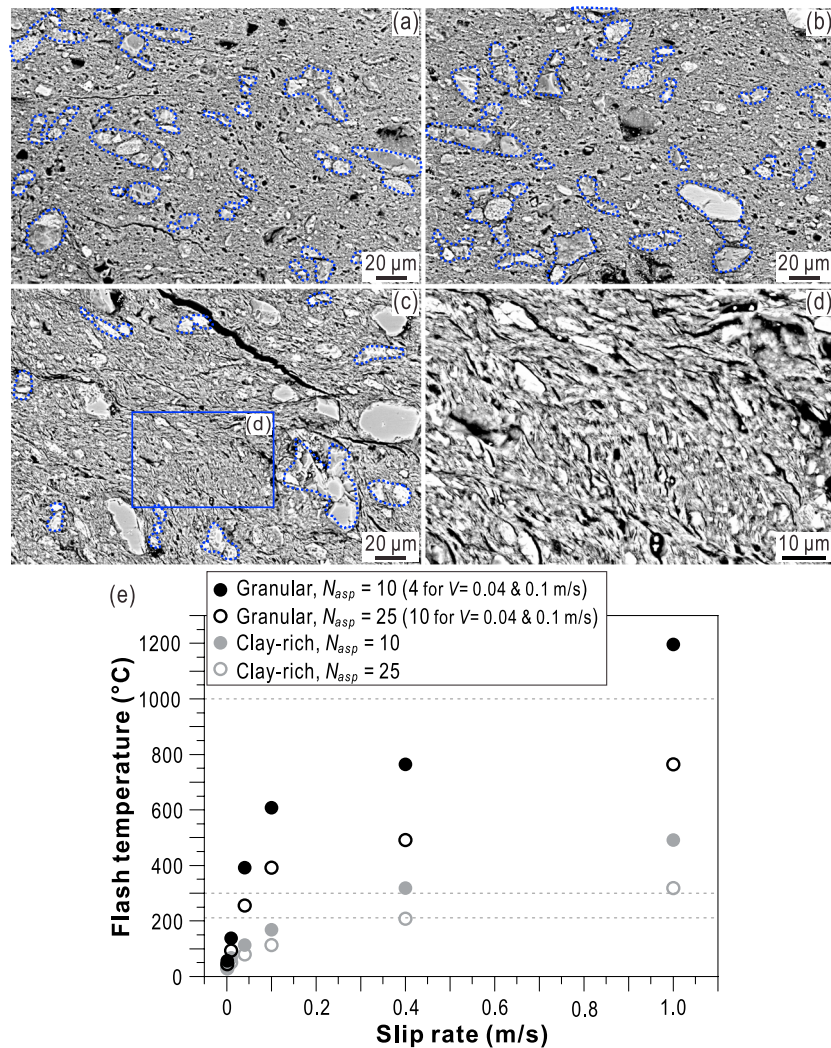


Figure 9. (a–d) Microstructures of the granular (a, b) and clay-rich (c, d) gouges sheared after the preslip. Dashed blue lines in the figures indicate the grains contacting with each other, which may act as asperity contacts during frictional sliding. (e) Maximum temperatures on the asperity contacts of the two gouges calculated with the equation (5) by using N_a (the number of contacts between which the total slip rate is shared) and other physical properties constrained from the mineral composition and microstructures.

To test our hypothesis, a helpful approach is to estimate the flash temperature rises in the experiments. We first reexamine the mineral composition and deformation textures of the gouges and constrain the key parameters in flash heating theory. For the granular gouge, the relatively hard minerals (69% in total) like quartz (20%) and plagioclase (18%) may act as strong framework supporting the force. This can be inferred from the visible grain size reduction through crushing of large grains (cf. Figures 5a and 5b–5h). Even in the slip zone of presheared gouge (Figures 9a and 9b), many grains are still in contact with each other (enclosed by dashed blue lines) and there is no clear shear texture in the fine grain matrix. Considering that τ_c of plagioclase and quartz are ~ 8 and ~ 9 – 12 GPa, respectively (Goldsby & Tullis, 2011), we adopt $\tau_c = 8$ GPa and $d = 5 \mu\text{m}$ for the granular gouge. The clay-rich gouge contains 65% phyllosilicates, 17% quartz, 13% plagioclase, and so on. Microstructures indicate that the clay minerals are highly sheared as suggested by strong foliations (Figures 9c and 9d). We assume $\tau_c = 2$ GPa and $d = 10 \mu\text{m}$ for the clay-rich gouge, considering that clay minerals mainly get involved in shear deformation and weak minerals tend to have larger contacts (though clay minerals themselves are fine, they may act as aggregates).

From one-dimensional thermal modeling with a Green's function approach, flash temperature on an asperity contact (T_a) within a gouge layer can be expressed as (Proctor et al., 2014)

$$T_a = T_f + \frac{\tau_c}{\rho C_p} \sqrt{\frac{(V/N_a)D_a}{\pi\alpha}}. \quad (5)$$

Here T_f , τ_c , ρ , C_p , V , N_a , D_a , and α are same quantities as those in the equation (3), and the (V/N_a) represents the slip velocity on a single asperity contact. As a first-order estimate, the latent heat of possible reactions is not considered in the equation (5). N_a is suggested to be around 10–20 (see Rice, 2006, section 1.1). Proctor et al. (2014) demonstrated that the V_w of serpentine gouges are 4–13 times higher than that of serpentine bare surfaces, indicating a possible N_a of 4–13 in their gouge experiments (Table 1 in Proctor et al., 2014). Similar values of N_a were also inferred from Yao et al. (2016). Here we assume $N_a = 4$ –10 in the cases of localized shear, namely, in the granular gouge experiments at $V = 0.04$ and 0.1 m/s, where ~40% of the gouge layer is involved in deformation (Figures 5e and 5f). By assuming similar spacing between asperity contacts, we use $N_a = 10$ –25 in the cases of distributed shear over the entire gouge layer (all other experiments; Figures 5c, 5d, 5g, 5h, and 6c–6f).

With above parameters and thermal properties (Table S1 in the supporting information), we calculated flash temperature rises of the two gouges at $V = 0.001, 0.01, 0.04, 0.1, 0.4,$ and 1.0 m/s at the onset of slip ($T_f = 20$ °C). The granular gouge gets visible T_a increases at $V \geq 0.04$ m/s, and the comparable T_a starts to emerge at $V \geq 0.4$ m/s for the clay-rich gouge (Figure 9e). This difference is partly due to the localized shear deformation for the granular gouge at $V = 0.04$ and 0.1 m/s. Note that the T_a at these two threshold velocities (0.04 vs. 0.4 m/s) are 255–392 °C and 209–319 °C (Figure 9e), respectively, which are close to the boiling point of water at pore pressure of 2 MPa (~212 °C). Then an open question is whether we can link the observed initial sharp weakening with flash heating in the case of the T_a down to ~200–400 °C, which is much lower than the T_w commonly believed.

As a key parameter in flash heating theory, T_w was originally considered as the characteristic temperature for melting on the contacts (Rice, 2006) and was later extended to the temperature for local softening due to thermally activated reactions such as thermal decomposition (e.g., Kohli et al., 2011; Tisato et al., 2012; Tullis, 2015). As we illustrated above, with T_w of 1000 °C for the granular gouge and of 300 °C for the clay-rich gouge, flash heating fails to explain the observed data of the granular gouge and could only partly explain the data of the clay-rich gouge (Figure 7). Since local melting and softening require high temperature, it is energetically more efficient to heat up and vaporize water layers or films on the asperity contact. If such a process occurs, the contact is likely to be lubricated with T_w as low as the boiling temperature of water (≥ 212 °C). To illustrate how effective flash weakening would be in this case, we compare the friction calculated by equations (3) and (4) with the same set of parameters except for different T_w (Figure 10). For the granular gouge, T_w of 212 °C makes big differences in the calculated friction (bold lines in Figure 10a as compared to thin lines for $T_w = 1000$ °C). Flash weakening with $T_w = 212$ °C could predict the rapid initial weakening and roughly the μ_{ss} levels at $V \geq 0.04$ m/s (measured data are shown in dashed lines). For the clay-rich gouge (Figure 10b), the calculated friction with $T_w = 212$ °C (bold lines) could better explain the initial weakening than that with $T_w = 300$ °C (thin lines) could do, although the model prediction in both cases are insufficient to interpret the measured data in the later stages (see further analysis below).

One may argue that the long preslip imposed may facilitate the formation of highly localized shear band, which could significantly promote flash heating and trigger rapid weakening, as demonstrated by Smith et al. (2015). In our experiments, while strain localization might occur in the preslip, it cannot be the main cause of the rapid weakening in the latter main slip. A strong evidence is that though the sheared dry gouge tends to have much narrower slip zones than wet gouges (cf. Figures 5 and S5; see also Togo et al., 2016), we still observe high friction in the control experiment under room humidity (with preslip; $V = 0.1$ m/s; Figure 4e), which is in contrast to rapid weakening in the wet tests at similar conditions.

Oohashi et al. (2015) have reported drastic slip weakening of water-saturated smectite-rich gouges at slip rates of ~0.01 m/s (using gabbro as host blocks), which is even slightly lower than the V_w of the granular gouge (0.04 m/s) observed in this study. They interpret that the dynamic weakening at intermediate velocities could be attributed to pore pressure increases caused by both shear-enhanced compaction and microscopic TP of pore fluids. Since the observed dynamic weakening distances are much smaller in our case and the compaction-induced pressurization is negligible during the initial weakening in our experiments, the underlying mechanisms responsible for the observed behaviors in the two studies are not exactly the same. In

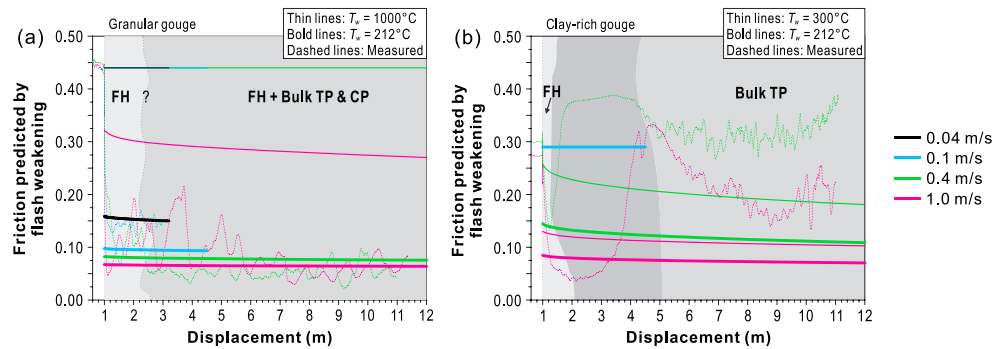


Figure 10. Friction evolution predicted by flash weakening with different characteristic weakening temperature. (a) Granular gouge and (b) clay-rich gouge. The possible weakening mechanism for each stage are marked in the figure (FH = flash heating; TP = thermal pressurization; CP = compaction-induced pressurization). The data measured in the experiments are shown in dashed lines for comparison. Colors of the lines denote slip rates.

principle, we agree with the concept in Oohashi et al. (2015) that flash heating may cause local vaporization of pore water on/around asperities. However, as is illustrated in Figure 10, we are inclined to believe that (1) the vaporization of water layers triggered by flash heating may change the contact status of asperities and weaken the asperity contacts directly (somewhat similar to the thermal softening process on asperities due to thermal decomposition). (2) TP due to local water vaporization seems to be the main reason for the observed instantaneous dilatancy during rapid weakening, but it probably only plays a secondary role in gouge weakening since the overall small area of true contacts may limit the macroscopic pressure rise.

The remaining problem is how to understand the differences between the two gouges in terms of the V_w and the evolution of friction at $V = 0.4\text{--}1.0$ m/s. First, flash heating operates through vaporization of water layers on contacts and results in rapid weakening soon after the sliding commences for both of the gouges (Figure 10). However, the contact shear strength and the shear zone width, which are relevant to mineral composition, may affect the efficiency of flash heating, local water vaporization, and TP, leading to the different V_w for the two gouges. Second, the later strengthening and weakening behaviors of the clay-rich gouge after the initial weakening ($V \geq 0.4$ m/s) are probably pertinent to the serious thermal expansion of the gouge layer (Figure 4b). Specifically, on the one hand, the thermal expansion may make contacts less stressed and deformation more distributed, and thus deactivate flash weakening and dilute the influence of local pressurization. On the other hand, bulk TP need some time to be activated since the porous host blocks were used. Therefore, the strengthening stage of the clay-rich gouge probably reflects a blank period for any weakening mechanisms. One may notice that the measured friction of the clay-rich gouge in the later stage is much higher than that from the model prediction (Figures 7b, 7d, and 10b). The main reason is that the possible increases in porosity, permeability, and asperity number during the serious thermal expansion, which may lower the efficiency of TP and flash heating, are not incorporated in the calculation due to lack of constraints on these parameters. In spite of the aforementioned discrepancy, the observed serious thermal expansion suggests that the later weakening stage of the clay-rich gouge (at displacements larger than 4 m) probably results from bulk TP (Figure 10b). In contrast, why the granular gouge maintains low friction ($V \geq 0.04$ m/s) may partly lie in its higher contact strength, thinner slip zones (Figures 5 and 9), and continuous axial shortening (Figures 4a and 4c; helpful to keep the gouge layer compact and contacts highly stressed), which could facilitate flash heating effectively. Moreover, the numerical modeling of bulk TP predicts considerable pore pressure rise in the later stage of experiments (especially at $V \geq 0.4$ m/s; Figure S3h), and the observed continuous shortening after the initial weakening may reflect further gouge compaction due to grain crushing (Figures 4a and 4c; cf. Figures 5b–5h). These analysis and observation suggest that both thermal and compaction-induced pressurization may also contribute to the weakening of the granular gouge during the later steady state sliding (Figure 10a).

7. Conclusions

In this research, we have uncovered the experimental evidence underpinning the importance of flash heating in dynamic weakening of water-saturated gouges. Low- to high-velocity (10 $\mu\text{m/s}$ to 1 m/s) friction

experiments were conducted on a granular gouge and a clay-rich gouge under water pressure of 2 MPa. The experiments were specially designed to dampen the effects of thermal and compaction-induced pressurization in the bulk gouge layer. Interesting findings are as follows:

1. Both of the granular and clay-rich gouges exhibit velocity strengthening at $V \leq 10\text{--}100$ mm/s and velocity weakening at $V \geq 0.04\text{--}0.4$ m/s. The velocity strengthening at low to intermediate velocities suggests the existence of a mechanical barrier to accelerating slip during earthquakes. The observed characteristic weakening velocity could be down to 0.04 m/s for the tested wet gouges, which is several times to an order of magnitude smaller than that for dry gouges.
2. The granular gouge shows drastic weakening at $V \geq 0.04$ m/s immediately after the sliding commences (<0.1 m of slip), and the clay-rich gouge shows similar rapid weakening at $V \geq 0.4$ m/s, followed by quick strengthening and modest weakening. The weakening distance for the initial drastic weakening is much smaller than previous reported values at similar experimental conditions. Furthermore, the initial drastic weakening is always contemporaneous with the instantaneous axial dilatancy of $10\text{--}25$ μm . Numerical modeling show that the initial drastic weakening cannot be interpreted as the consequence of bulk TP and flash weakening through local melting or softening on asperity contacts.
3. Flash temperature calculation integrated with microstructural observation suggest that the vaporization of water films (layers) on/around the contacts caused by flash heating may lubricate the asperity contacts. This could trigger flash weakening at the contact temperature much lower than that commonly recognized (≥ 212 $^{\circ}\text{C}$ in our case). This process and local pressurization may cause the sudden initial weakening and contemporaneous dilatancy for the two gouges at subseismic to seismic slip rates. The differences in the efficiency of flash heating could explain the different frictional behaviors of the two gouges in terms of the characteristic weakening velocities and overall friction evolution at seismic slip rates. As flash weakening triggered by water vaporization is very efficient, the fluid-infiltrated faults could be weakened more rapidly than previously recognized during earthquakes, which may significantly promote dynamic rupture propagation.

Acknowledgments

This work was supported by the International Science and Technology Cooperation Program of China (grant 2011DFG23400), the National Natural Science Foundation of China (grants 41774191 and 41404143), and the State Key Laboratory of Earthquake Dynamics (grant LED2014A06). We sincerely thank Kiyokazu Ohashi and an anonymous reviewer for their thoughtful and detailed comments and the editor Yehuda Ben-Zion and the associate editor for evaluating our manuscript. We also thank Lei Zhang, Tetsuhiro Togo, Hiroko Kitajima, Yu Wang, and Haoyue Sun for their help in the field. Qingbao Duan, Zihua Tang, and Yongda Wang are thanked for their help in measuring permeability and grain size. The authors have no financial conflict of interest. All the presented data in this paper are available in the supporting information.

References

- Beeler, N. M., Tullis, T. E., & Goldsby, D. L. (2008). Constitutive relationships and physical basis of fault strength due to flash heating. *Journal of Geophysical Research*, *113*, B01401. <https://doi.org/10.1029/2007jb004988>
- Boulton, C., Yao, L., Faulkner, D. R., Townend, J., Toy, V. G., Sutherland, R., et al. (2017). High-velocity frictional properties of Alpine Fault rocks: Mechanical data, microstructural analysis, and implications for rupture propagation. *Journal of Structural Geology*, *97*, 71–92. <https://doi.org/10.1016/j.jsg.2017.02.003>
- Brace, W. F., Walsh, J. B., & Frangos, W. T. (1968). Permeability of granite under high pressure. *Journal of Geophysical Research*, *73*(6), 2225–2236. <https://doi.org/10.1029/JB073i006p02225>
- Brantut, N., & Platt, J. D. (2017). Dynamic weakening and the depth dependence of earthquake faulting. In M. Y. Thomas, T. M. Mitchell, & H. S. Bhat (Eds.), *Fault zone dynamic processes: Evolution of fault properties during seismic rupture*, *Geophys. Monogr. Ser.*, (pp. 171–194). Washington, DC: American Geophysical Union. <https://doi.org/10.1002/9781119156895.ch9>
- Brantut, N., Schubnel, A., Corvisier, J., & Sarout, J. (2010). Thermochemical pressurization of faults during coseismic slip. *Journal of Geophysical Research*, *115*, B05314. <https://doi.org/10.1029/2009jb006533>
- Brigaud, F., & Vasseur, G. (1989). Mineralogy, porosity and fluid control on thermal conductivity of sedimentary rocks. *Geophysical Journal*, *98*(3), 525–542. <https://doi.org/10.1111/j.1365-246X.1989.tb02287.x>
- Buijze, L., Niemeijer, A. R., Han, R., Shimamoto, T., & Spiers, C. J. (2017). Friction properties and deformation mechanisms of halite-(mica) gouges from low to high sliding velocities. *Earth and Planetary Science Letters*, *458*, 107–119. <https://doi.org/10.1016/j.epsl.2016.09.059>
- Chen, J., Niemeijer, A. R., & Fokker, P. A. (2017). Vaporization of fault water during seismic slip. *Journal of Geophysical Research: Solid Earth*, *122*, 4237–4276. <https://doi.org/10.1002/2016JB013824>
- Chen, J., Niemeijer, A. R., Yao, L., & Ma, S. (2017). Water vaporization promotes coseismic fluid pressurization and buffers temperature rise. *Geophysical Research Letters*, *44*, 2177–2185. <https://doi.org/10.1002/2016GL071932>
- Chen, J., Yang, X., Duan, Q., Shimamoto, T., & Spiers, C. J. (2013). Importance of thermochemical pressurization in the dynamic weakening of the Longmenshan Fault during the 2008 Wenchuan earthquake: Inferences from experiments and modeling. *Journal of Geophysical Research: Solid Earth*, *118*, 4145–4169. <https://doi.org/10.1002/jgrb.50260>
- Chen, J., Yang, X., Yao, L., Ma, S., & Shimamoto, T. (2013). Frictional and transport properties of the 2008 Wenchuan earthquake fault zone: Implications for coseismic slip-weakening mechanisms. *Tectonophysics*, *603*, 237–256. <https://doi.org/10.1016/j.tecto.2013.05.035>
- Clauser, C., & Huenges, E. (1995). Thermal conductivity of rocks and minerals. In T. J. Ahrens (Ed.), *Rock physics and phase relations: A handbook of physical constants*, *AGU Ref. Shelf. Ser.*, (Vol. 3, pp. 105–126). Washington, DC: American Geophysical Union. <https://doi.org/10.1029/RF003p0105>
- Faulkner, D. R., Mitchell, T. M., Behn, S. J., Hirose, T., & Shimamoto, T. (2011). Stuck in the mud? Earthquake nucleation and propagation through accretionary forearcs. *Geophysical Research Letters*, *38*, L18303. <https://doi.org/10.1029/2011gl048552>
- Ferri, F., Di Toro, G., Hirose, T., Han, R., Noda, H., Shimamoto, T., et al. (2011). Low- to high-velocity frictional properties of the clay-rich gouges from the slipping zone of the 1963 Vaiont slide, northern Italy. *Journal of Geophysical Research*, *116*, B09208. <https://doi.org/10.1029/2011jb008338>

- Ferri, F., Di Toro, G., Hirose, T., & Shimamoto, T. (2010). Evidence of thermal pressurization in high-velocity friction experiments on smectite-rich gouges. *Terra Nova*, 22(5), 347–353. <https://doi.org/10.1111/j.1365-3121.2010.00955.x>
- Fujiwara, T., Kodaira, S., No, T., Kaiho, Y., Takahashi, N., & Kaneda, Y. (2011). The 2011 Tohoku-Oki earthquake: Displacement reaching the trench axis. *Science*, 334(6060), 1240–1240. <https://doi.org/10.1126/science.1211554>
- Fulton, P. M., Brodsky, E. E., Kano, Y., Mori, J., Chester, F., Ishikawa, T., et al. (2013). Low coseismic friction on the Tohoku-Oki fault determined from temperature measurements. *Science*, 342(6163), 1214–1217. <https://doi.org/10.1126/science.1243641>
- Goldsby, D. L., & Tullis, T. E. (2011). Flash heating leads to low frictional strength of crustal rocks at earthquake slip rates. *Science*, 334(6053), 216–218. <https://doi.org/10.1126/science.1207902>
- Kitajima, H., Chester, F. M., & Chester, J. S. (2011). Dynamic weakening of gouge layers in high-speed shear experiments: Assessment of temperature-dependent friction, thermal pressurization, and flash heating. *Journal of Geophysical Research*, 116, B08309. <https://doi.org/10.1029/2010jb007879>
- Kohli, A. H., Goldsby, D. L., Hirth, G., & Tullis, T. (2011). Flash weakening of serpentinite at near-seismic slip rates. *Journal of Geophysical Research*, 116, B03202. <https://doi.org/10.1029/2010JB007833>
- Lambe, T. W., & Whitman, R. (1969). *Soil mechanics*, (p. 553). New York: John Wiley.
- Li, H., Xue, L., Brodsky, E. E., Mori, J. J., Fulton, P. M., Wang, H., et al. (2015). Long-term temperature records following the M_w 7.9 Wenchuan (China) earthquake are consistent with low friction. *Geology*, 43(2), 163–166. <https://doi.org/10.1130/g35515.1>
- Liu-Zeng, J., Zhang, Z., Wen, L., Tapponnier, P., Sun, J., Xing, X., et al. (2009). Co-seismic ruptures of the 12 May 2008, M_s 8.0 Wenchuan earthquake, Sichuan: East-west crustal shortening on oblique, parallel thrusts along the eastern edge of Tibet. *Earth and Planetary Science Letters*, 286(3–4), 355–370. <https://doi.org/10.1016/j.epsl.2009.07.017>
- Ma, S., Shimamoto, T., Yao, L., Togo, T., & Kitajima, H. (2014). A rotary-shear low to high-velocity friction apparatus in Beijing to study rock friction at plate to seismic slip rates. *Earthquake Science*, 27(5), 469–497. <https://doi.org/10.1007/s11589-014-0097-5>
- Marone, C., Raleigh, C., & Scholz, C. (1990). Frictional behavior and constitutive modeling of simulated fault gouge. *Journal of Geophysical Research*, 95(B5), 7007–7025. <https://doi.org/10.1029/JB095iB05p07007>
- Mizoguchi, K., Hirose, T., Shimamoto, T., & Fukuyama, E. (2006). Moisture-related weakening and strengthening of a fault activated at seismic slip rates. *Geophysical Research Letters*, 33, L16319. <https://doi.org/10.1029/2006gl026980>
- Noda, H., & Shimamoto, T. (2005). Thermal pressurization and slip-weakening distance of a fault: An example of the Hanaore fault, Southwest Japan. *Bulletin of the Seismological Society of America*, 95(4), 1224–1233. <https://doi.org/10.1785/0120040089>
- Oohashi, K., Hirose, T., & Shimamoto, T. (2011). Shear-induced graphitization of carbonaceous materials during seismic fault motion: Experiments and possible implications for fault mechanics. *Journal of Structural Geology*, 33(6), 1122–1134. <https://doi.org/10.1016/j.jsg.2011.01.007>
- Oohashi, K., Hirose, T., Takahashi, M., & Tanikawa, W. (2015). Dynamic weakening of smectite-bearing faults at intermediate velocities: Implications for subduction zone earthquakes. *Journal of Geophysical Research: Solid Earth*, 120, 1572–1586. <https://doi.org/10.1002/2015JB011881>
- Passelègue, F. X., Goldsby, D. L., & Fabbri, O. (2014). The influence of ambient fault temperature on flash-heating phenomena. *Geophysical Research Letters*, 41, 828–835. <https://doi.org/10.1002/2013GL058374>
- Platt, J., B. Proctor, T. Mitchell, G. Hirth, D. Goldsby, G. Di Toro, et al. (2014). The role of gouge and temperature on flash heating and its hysteresis. Abstract S11C–4360 presented at 2014 Fall Meeting, AGU, San Francisco, California, December 15–19.
- Proctor, B. P., Mitchell, T. M., Hirth, G., Goldsby, D., Zorzi, F., Platt, J. D., & et al. (2014). Dynamic weakening of serpentinite gouges and bare surfaces at seismic slip rates. *Journal of Geophysical Research: Solid Earth*, 119, 8107–8131. <https://doi.org/10.1002/2014JB011057>
- Reches, Z. E., & Lockner, D. A. (2010). Fault weakening and earthquake instability by powder lubrication. *Nature*, 467(7314), 452–455. <https://doi.org/10.1038/nature09348>
- Rempel, A. W. (2006). The effects of flash-weakening and damage on the evolution of fault strength and temperature. In R. Abercrombie, A. McGarr, G. Di Toro, & H. Kanamori (Eds.), *Earthquakes: Radiated energy and the physics of faulting*, *Geophys. Monogr. Ser.*, (Vol. 170, pp. 263–270). Washington, DC: American Geophysical Union. <https://doi.org/10.1029/170GM26>
- Rice, J. R. (2006). Heating and weakening of faults during earthquake slip. *Journal of Geophysical Research*, 111, B05311. <https://doi.org/10.1029/2005jb004006>
- Robertson, E. C. (1988). Thermal properties of rocks. U.S. Geological Survey.
- Sammis, C., Lockner, D., & Reches, Z. E. (2011). The role of adsorbed water on the friction of a layer of submicron particles. *Pure and Applied Geophysics*, 168(12), 2325–2334. <https://doi.org/10.1007/s00024-011-0324-0>
- Sawai, M., Hirose, T., & Kameda, J. (2014). Frictional properties of incoming pelagic sediments at the Japan trench: Implications for large slip at a shallow plate boundary during the 2011 Tohoku earthquake. *Earth, Planets and Space*, 66(1), 65–68. <https://doi.org/10.1186/1880-5981-66-65>
- Schön, J. (2011). Physical Properties of Rocks - A Workbook. In *Handbook of Petroleum Exploration and Production* (Vol. 8). Elsevier.
- Segall, P., & Rice, J. R. (1995). Dilatancy, compaction, and slip instability of a fluid-infiltrated fault. *Journal of Geophysical Research*, 100(B11), 22,155–22,171. <https://doi.org/10.1029/95jb02403>
- Skauge, A., Fuller, N., & Hepler, L. G. (1983). Specific heats of clay minerals: Sodium and calcium kaolinites, sodium and calcium montmorillonites, illite, and attapulgite. *Thermochimica Acta*, 61(1–2), 139–145.
- Smith, S. A. F., Nielsen, S., & Di Toro, G. (2015). Strain localization and the onset of dynamic weakening in calcite fault gouge. *Earth and Planetary Science Letters*, 413(2015), 25–36. <https://doi.org/10.1016/j.epsl.2014.12.043>
- Spagnuolo, E., Plümpner, O., Violay, M., Cavallo, A., & Di Toro, G. (2015). Fast-moving dislocations trigger flash weakening in carbonate-bearing faults during earthquakes. *Scientific Reports*, 5(1), 16112. <https://doi.org/10.1038/srep16112>
- Sun, H., He, H., Ikeda, Y., Kano, K. i., Shi, F., Gao, W., et al. (2015). Holocene paleoearthquake history on the Qingchuan fault in the northeastern segment of the Longmenshan thrust zone and its implications. *Tectonophysics*, 660, 92–106. <https://doi.org/10.1016/j.tecto.2015.08.022>
- Tanikawa, W., Sakaguchi, M., Hirono, T., Lin, W., Soh, W., & Song, S.-R. (2009). Transport properties and dynamic processes in a fault zone from samples recovered from TCDP Hole B of the Taiwan Chelungpu fault Drilling Project. *Geochemistry, Geophysics, Geosystems*, 10, Q04013. <https://doi.org/10.1029/2008gc002269>
- Tisato, N., Di Toro, G., De Rossi, N., Quaresimin, M., & Candela, T. (2012). Experimental investigation of flash weakening in limestone. *Journal of Structural Geology*, 38, 183–199. <https://doi.org/10.1016/j.jsg.2011.11.017>
- Togo, T., Shimamoto, T., Ma, S., & Hirose, T. (2011). High-velocity frictional behavior of Longmenshan fault gouge from Hongkou outcrop and its implications for dynamic weakening of fault during the 2008 Wenchuan earthquake. *Earthquake Science*, 24(3), 267–281. <https://doi.org/10.1007/s11589-011-0790-6>

- Togo, T., Yao, L., Ma, S., & Shimamoto, T. (2016). High-velocity frictional strength of Longmenshan fault gouge and its comparison with an estimate of friction from the temperature anomaly in WFS-1 drill hole. *Journal of Geophysical Research: Solid Earth*, *121*, 5328–5348. <https://doi.org/10.1002/2016JB012880>
- Tullis, T. E. (2015). Mechanisms for friction of rock at earthquake slip rates. In G. Schubert (Ed.), *Treatise on Geophysics*, (2nd ed., pp. 139–159). Oxford: Elsevier. <https://doi.org/10.1016/B978-0-444-53802-4.00073-7>
- Ujii, K., Tanaka, H., Saito, T., Tsutsumi, A., Mori, J. J., Kameda, J., et al. (2013). Low Coseismic shear stress on the Tohoku-Oki megathrust determined from laboratory experiments. *Science*, *342*(6163), 1211–1214. <https://doi.org/10.1126/science.1243485>
- Ujii, K., & Tsutsumi, A. (2010). High-velocity frictional properties of clay-rich fault gouge in a megasplay fault zone, Nankai subduction zone. *Geophysical Research Letters*, *37*, L24310. <https://doi.org/10.1029/2010gl046002>
- Violay, M., Di Toro, G., Nielsen, S., Spagnuolo, E., & Burg, J. P. (2015). Thermo-mechanical pressurization of experimental faults in cohesive rocks during seismic slip. *Earth and Planetary Science Letters*, *429*, 1–10. <https://doi.org/10.1016/j.epsl.2015.07.054>
- Viti, C., & Hirose, T. (2010). Thermal decomposition of serpentine during coseismic faulting: Nanostructures and mineral reactions. *Journal of Structural Geology*, *32*(10), 1476–1484. <https://doi.org/10.1016/j.jsg.2010.09.009>
- Waples, D. W., & Waples, J. S. (2004). A review and evaluation of specific heat capacities of rocks, minerals, and subsurface fluids. Part 1: Minerals and nonporous rocks. *Natural Resources Research*, *13*(2), 97–122. <https://doi.org/10.1023/B:NARR.0000032647.41046.e7>
- Wibberley, C. A. J., & Shimamoto, T. (2005). Earthquake slip weakening and asperities explained by thermal pressurization. *Nature*, *436*(7051), 689–692. <https://doi.org/10.1038/nature03901>
- Yao, L., Ma, S., Platt, J. D., Niemeijer, A. R., & Shimamoto, T. (2016). The crucial role of temperature in high-velocity weakening of faults: Experiments on gouge using host blocks with different thermal conductivities. *Geology*, *44*(1), 63–66. <https://doi.org/10.1130/g37310.1>
- Yao, L., Ma, S., Shimamoto, T., & Togo, T. (2013). Structures and high-velocity frictional properties of the Pingxi fault zone in the Longmenshan fault system, Sichuan, China, activated during the 2008 Wenchuan earthquake. *Tectonophysics*, *599*, 135–156. <https://doi.org/10.1016/j.tecto.2013.04.011>
- Zhang, L., & He, C. (2013). Frictional properties of natural gouges from Longmenshan fault zone ruptured during the Wenchuan Mw7.9 earthquake. *Tectonophysics*, *594*, 149–164. <https://doi.org/10.1016/j.tecto.2013.03.030>